

# Whole-brain diffusional variance decomposition (DIVIDE): Demonstration of technical feasibility at clinical MRI systems

Filip Szczepankiewicz<sup>1</sup>, Jens Sjölund<sup>2,3,4</sup>, Freddy Ståhlberg<sup>1,5,6</sup>, Jimmy Lätt<sup>7</sup>, Markus Nilsson<sup>5,6</sup>

1. Lund University, Department of Clinical Sciences Lund, Medical Radiation Physics, Lund, Sweden; 2. Elekta Instrument AB, Kungstengsgatan 18, Box 7593, SE-103 93 Stockholm, Sweden; 3. Department of Biomedical Engineering, Linköping University, Linköping, Sweden; 4. Center for Medical Image Science and Visualization (CMIV), Linköping University, Sweden; 5. Lund University, Skåne University Hospital, Department of Clinical Sciences Lund, Diagnostic Radiology, Lund, Sweden; 6. Lund University, Lund University Bioimaging Center, Lund, Sweden; 7. Skåne University Hospital, Department of Imaging and Function, Lund, Sweden.

## Abstract

*Purpose:* To assess the technical feasibility of whole-brain diffusional variance decomposition (DIVIDE) based on q-space trajectory encoding (QTE) at clinical MRI systems with varying performance. DIVIDE is used to separate diffusional heterogeneity into components that arise due to isotropic and anisotropic tissue structures.

*Methods:* We designed imaging protocols for DIVIDE using numerically optimized gradient waveforms for diffusion encoding. Imaging was performed at systems with magnetic field strengths between 1.5 and 7 T, and gradient amplitudes between 33 and 80 mT/m. Technical feasibility was assessed from signal characteristics and quality of parameter maps in a single volunteer scanned at all systems.

*Results:* The technical feasibility of QTE and DIVIDE was demonstrated at all systems. The system with the highest performance allowed whole-brain DIVIDE at 2 mm isotropic voxels. The system with the lowest performance required a spatial resolution of  $2.5 \times 2.5 \times 4 \text{ mm}^3$  to yield a sufficient signal-to-noise ratio.

*Conclusions:* Whole-brain DIVIDE based on QTE is feasible at the investigated MRI systems. This demonstration indicates that tissue features beyond those accessible by conventional diffusion encoding may be explored on a wide range of MRI systems.

## Introduction

Diffusion MRI (dMRI) enables non-invasive imaging of tissue microstructure. Methods such as diffusion tensor imaging (DTI) (Basser et al., 1994) yield parameters which are sensitive to alterations of the tissue microstructure in both healthy development and disease (Assaf and Pasternak, 2008). However, DTI captures only a voxel-scale average, whereas quantification of diffusion heterogeneity on the sub-voxel scale warrants the use of multiple b-values and methods capable of analyzing such data. Diffusional kurtosis imaging (DKI) (Jensen et al., 2005) is an extension to DTI that can probe sub-voxel heterogeneity, which may be of importance in, for example, tumor imaging. Accordingly, several studies have found that DKI is better at differentiating high and low grade gliomas compared to DTI; presumably due to its sensitivity to tissue heterogeneity (Raab et al., 2010, Van Cauter et al., 2012). However, DTI and DKI, along with the vast majority of other dMRI techniques, are based on so-called single diffusion encoding (SDE), i.e. a pair of pulsed gradients that encode for diffusion along a single direction per acquisition (Stejskal and Tanner, 1965). Notably, methods based solely on SDE data are inherently limited since they will inadvertently conflate two separate components of heterogeneity corresponding to either microscopic anisotropy or isotropic heterogeneity (Mitra, 1995, Szczepankiewicz et al., 2016a).

A promising solution to disambiguate the two components of heterogeneity is to probe the diffusion in more than one direction in a single shot, i.e. encoding that yields b-tensors of rank two or three (Westin et al., 2016). A prominent example is double diffusion encoding (DDE), which can produce b-tensors of rank one or two and thereby disambiguate the two tissue characteristics conflated by SDE (Cory et al., 1990, Özarıslan and Basser, 2008, Shemesh et al., 2010). Beyond the paradigm of pulsed gradients used in SDE and DDE, is q-space trajectory encoding (QTE), which is not constrained to pulsed gradients and can render b-tensors of rank one, two or three, e.g. linear, planar or spherical encoding (Lasič et al., 2014, Eriksson et al., 2015, Topgaard, 2016, Westin et al., 2016). We recently demonstrated that a combination of linear and spherical b-tensor encoding (LTE and STE) can be used to disambiguate microscopic anisotropy from orientation coherence by so-called diffusional variance decomposition (DIVIDE) (Szczepankiewicz et al., 2015). DIVIDE has also been used in brain tumors to separate effects of cell eccentricity and variable cell density (Szczepankiewicz et al., 2016a). In conventional DKI (Jensen et al., 2005, Jensen and Helpert, 2010), these two fundamentally different sources of diffusional variance are not separable (Szczepankiewicz et al., 2016a).

The concept of diffusional variance employed in DIVIDE, and its relation to tissue heterogeneity, can be

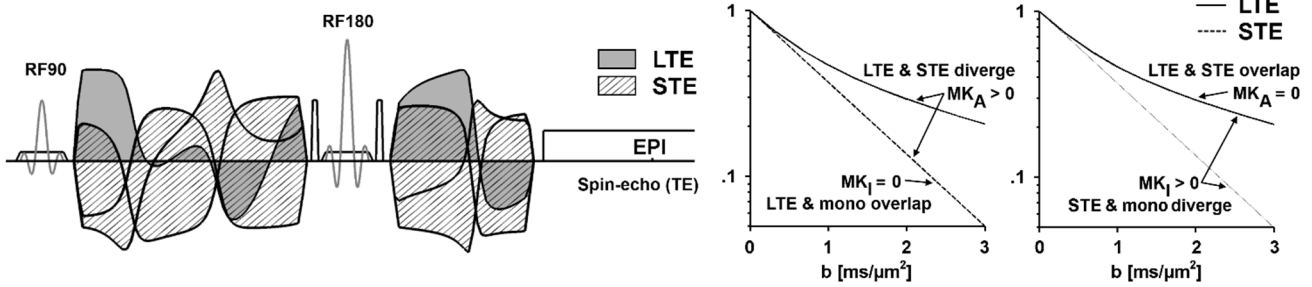


Figure 1 | Schematic spin-echo sequence with echo planar imaging (EPI) readout, and signal vs.  $b$  curves in two toy examples (right). The pulse sequence depicts gradients that yield linear and spherical b-tensor encoding (LTE and STE). The gradients can be asymmetric around the refocusing pulse (Sjölund et al., 2015). In the first toy example (left signal plot), we assume a tissue comprising randomly oriented and anisotropic diffusion tensors (microscopic anisotropy). In the second example, it comprises isotropic tensors with two distinct diffusivities (isotropic heterogeneity). Even if the underlying tissue is markedly different, the LTE signal is the same in both examples. However, they can be distinguished by also using STE. In the first case, the LTE and STE signal diverge (hallmark of anisotropic variance), and the STE signal is monoexponential (no isotropic variance). In the second case, the LTE and STE signals overlap (no anisotropic variance) and the STE signal is non-monoexponential (hallmark of isotropic variance).

understood by considering that, at low  $b$ -values ( $b < 1 \text{ ms}/\mu\text{m}^2 = 1000 \text{ s}/\text{mm}^2$ ), the diffusion-weighted signal depends primarily on the apparent diffusion coefficient (ADC) (Le Bihan, 2013, Jensen, 2014). The ADC reflects the average apparent diffusivity in a voxel, and is sensitive to a range of different microstructure features, for example, anisotropy in white matter (Basser and Pierpaoli, 1996) or the cell density in tumors (Chen et al., 2013). At moderate  $b$ -values ( $b < 3 \text{ ms}/\mu\text{m}^2$ ), the signal will depend on the average diffusivity as well as the heterogeneity of the intra-voxel distribution of diffusion coefficients (DDC) (Callaghan and Pinder, 1983), i.e. the so-called diffusional variance (Yablonskiy et al., 2003, Jensen et al., 2005). By employing multiple b-tensors, e.g. LTE and STE, it is possible to decompose the diffusional variance into components caused by isotropic and anisotropic features of the microstructure (Lasič et al., 2014, Szczepankiewicz et al., 2015, Szczepankiewicz et al., 2016a). Figure 1 shows how the diffusion-weighted signal depends on anisotropic and isotropic diffusional variance when using LTE and STE.

The drawback of encoding with b-tensors of rank above one is that they are generally more demanding with respect to hardware performance, compared to conventional SDE. As such, these techniques have been developed and used primarily at high-performance MRI systems that facilitate sufficient data quality and acceptable acquisition times. For example, the initial implementation of DIVIDE was performed at a 3 T scanner with 80 mT/m gradients. Even so, it required an echo time of 160 ms to achieve a  $b$ -value of  $2.8 \text{ ms}/\mu\text{m}^2$ , which limited the spatial resolution and coverage (Szczepankiewicz et al., 2015). Due to the low signal-to-noise ratio imposed by long echo times, the technical feasibility for whole-brain DIVIDE at lower field strengths and/or gradient amplitudes, in clinically acceptable times, is not obvious. However, recent

development of numerically optimized waveforms has facilitated improved encoding efficiency enabling QTE at substantially shorter echo times (Sjölund et al., 2015). This development allows for faster acquisitions and higher SNR, and motivates an investigation of the technical feasibility of QTE and DIVIDE on a wider range of systems.

The aim of this study was to survey the technical feasibility of QTE and whole-brain DIVIDE at a wide range of MRI systems, covering field strengths between 1.5 and 7 T, and gradient amplitudes between 33 and 80 mT/m. We expected a nearly linear dependency of SNR on field strength (Moser et al., 2012). However, higher SNR is not guaranteed at 7 T because the transversal relaxation time is substantially shorter which may decrease the SNR given long enough echo times (Cox and Gowland, 2010, Choi et al., 2011, Szczepankiewicz et al., 2016b). Similarly, we expected the SNR to increase with gradient performance, since stronger gradients results in shorter echo times for any a given  $b$ -value. The results showed that whole-brain DIVIDE based on QTE is feasible at all investigated systems, although the spatial resolution should be reduced at some systems to accommodate the lower SNR resulting from low field strength and/or gradient amplitude.

## Methods

We investigated the technical feasibility of DIVIDE at MRI systems with multiple field strengths ( $B_0 = 1.5, 3, \text{ and } 7 \text{ T}$ ) and maximal gradient amplitudes ( $G_{\text{max}} = 33, 45, 60, \text{ and } 80 \text{ mT/m}$ ). An overview of the systems is found in Table 1. Note that systems A and B are the same physical scanner, but that system A was artificially limited to yield a maximal gradient amplitude of 33 mT/m.

The QTE sequence was deemed technically feasible if it produced data with whole-brain coverage (120 mm contiguous coverage in feet-head direction), in-plane

resolution of  $2 \times 2 \text{ mm}^2$ , slice thickness of 4 mm, SNR above 3 at the highest b-value, and DIVIDE parameter maps without prominent artefacts, in less than 8 minutes.

The software used for the model fitting and waveform optimization was implemented in Matlab (The Mathworks, Natick, MA) and is available at <https://github.com/markus-nilsson/md-dmri>.

#### Protocol design and data acquisition

The protocols were designed using heuristic guidelines in a procedure that followed three steps: (i) determine the minimal and maximal b-values, (ii) determine the minimal echo and repetition times (TE and TR), as well as the maximal number of samples, and (iii) distribute the samples across b-tensors, b-values and encoding directions. Details for each step are given in the appendix. Protocols were adapted for each system, and are summarized in Table 1. Independent of MRI system, the following imaging parameters were kept constant: acquisition matrix  $256 \times 256 \times 30$ , partial Fourier 0.75, strong fat suppression, parallel acceleration factor 2, bandwidth 1400 Hz/voxel. Notably, the default spatial resolution was  $2 \times 2 \times 4 \text{ mm}^3$ . The impact of anisotropic voxels is commented on in the discussion.

QTE with optimized waveforms was used to achieve high encoding efficacy, and therefore high SNR. The QTE sequence was based on the spin-echo diffusion-weighting sequence provided by Philips Healthcare (Best, the Netherlands) and Siemens Healthcare (GmbH, Erlangen, Germany), and developed in the pulse programming environment provided by each vendor. Gradient waveforms were optimized based on the specifications of

each MRI system (Sjölund et al., 2015). Briefly, the optimization used the Euclidean norm to create rotatable waveforms, a heat dissipation factor of  $\eta = 0.9$ , and a slew rate limitations of 100 T/m/s to reduce peripheral nerve stimulation (Ham et al., 1997, Hebrank and Gebhardt, 2000). The LTE waveform was calculated from the STE waveform, such that it had the same q-vector magnitude as a function of time, according to Lasič et al. (2014). An example of a spin-echo sequence with an optimized gradient waveform is shown in Figure 1.

All data was acquired in the same healthy volunteer (male, 35 y) on all systems. All experiments were approved by the Regional Ethical Review Board, and informed consent was obtained prior to participation. Diffusion weighted data was corrected for motion and eddy-currents in Elastix (Klein et al., 2010) using an extrapolation-based reference volume (Nilsson et al., 2015). No smoothing of data was used, in order to retain the impact of signal noise on the images.

All protocols yielded whole-brain coverage in under 8 minutes. However, the system with lowest performance (system A) did not pass our criteria for technical feasibility due to low SNR. Thus, we investigated the necessary reduction in spatial resolution that would compensate for the low SNR. For this protocol, the matrix size was  $102 \times 102 \times 30$ , and the bandwidth was reduced to 1150 Hz/voxel to yield the same readout time. Conversely, at the system with highest performance (system D), we investigated the feasibility of increasing the resolution to 2 mm isotropic voxels, changing only the repetition time to 8400 ms, yielding an acquisition time of 16 minutes.

Table 1 – Hardware specification, imaging protocols, and quality parameters at all systems. Systems A-D used 20-channel receive head/neck-coil arrays. System E used a 32 channel transmit/receive head-coil array. All protocols used equidistant b-values in the interval  $[0.1, 2] \text{ ms}/\mu\text{m}^2$ . For example, four b-shells yield  $b \approx 0.1, 0.7, 1.4, \text{ and } 2 \text{ ms}/\mu\text{m}^2$ .

Hardware		A <sup>†</sup>	B <sup>‡</sup>	C <sup>‡</sup>	D <sup>*</sup>	E <sup>**</sup>
$B_0$	T	1.5	1.5	3.0	3.0	7.0
$G_{\text{max}}$	mT/m	33	45	45	80	60
$S_{\text{max}}$	T/m/s	125	200	200	200	100
Coil-Ch		20	20	20	20	32
Protocol						
TE	ms	138	120	120	91	99
TR	ms	5600	5000	5000	4200	5000
$\delta_1, \delta_2$	ms	60, 51	51, 43	51, 43	35, 26	41, 32
b-shells		3	4	4	5	4
$n_{\text{dir}}$		7, 12, 20	6, 6, 12, 19	6, 6, 12, 19	6, 6, 10, 11, 20	6, 6, 12, 20
$T_{\text{tot}}$	min	7:50	7:50	7:50	7:58	8:00
Quality						
$Q_3$	%	88	97	99	100	95
$Q_6$	%	12	29	69	94	69

<sup>†</sup> Siemens Magnetom Aera; <sup>‡</sup> Siemens Magnetom Skyra; <sup>\*</sup> Siemens Magnetom Prisma; <sup>\*\*</sup> Philips Achieva.  $B_0$  main magnetic field strength;  $G_{\text{max}}$  maximum gradient amplitude;  $S_{\text{max}}$  maximum gradient slew rate; TE echo time; TR repetition time;  $\delta_1$  and  $\delta_2$  duration of waveform before and after refocusing pulse;  $n_{\text{dir}}$  number of directions in each b-shell;  $T_{\text{tot}}$  total acquisition time including preparation stage;  $Q_3$  and  $Q_6$  fraction of tissue where SNR is above 3 and 6 at  $b = 2 \text{ ms}/\mu\text{m}^2$ .

### Parameter estimation

DIVIDE employs a joint analysis of LTE and STE data to disentangle the anisotropic and isotropic diffusional variance ( $V_A$  and  $V_I$ ). We used the inverse Laplace transform of the gamma distribution as a signal model (Jensen and Helpert, 2010, Röding et al., 2012), in accordance with previous implementations (Lasič et al., 2014, Szczepankiewicz et al., 2015). The gamma distribution is described by two parameters that correspond to the expected value (MD) and variance ( $V_{DDC}$ ) of the DDC {Jensen, 2010 #231}, which gives an expression for the signal, according to

$$S(b, b_\Delta) = S_0 \cdot \left(1 + b \cdot \frac{V_{DDC}}{MD}\right)^{-\frac{MD^2}{V_{DDC}}}, \quad \text{Eq. 1}$$

where  $S_0$  is the signal at  $b = 0 \text{ ms}/\mu\text{m}^2$ , and the observed diffusional variance ( $V_{DDC}$ ) depends on the b-tensor anisotropy ( $b_\Delta$ ),

$$V_{DDC} = V_I + b_\Delta^2 \cdot V_A, \quad \text{Eq. 2}$$

with  $b_\Delta = 0$  for STE and  $b_\Delta = 1$  for LTE (Eriksson et al., 2015, Topgaard, 2016). To obtain rotation invariant parameters in anisotropic samples, such as neural tissue, we performed so-called ‘powder averaging’ (Bak and Nielsen, 1997, Edén, 2003). The powder averaged signal ( $\bar{S}$ ) is defined as the arithmetic average of the diffusion-weighted signal across all diffusion encoding directions in a given b-shell. The encoding directions are uniformly distributed on the half-sphere using an electrostatic repulsion model (Jones et al., 1999). Parameters were estimated by fitting Eq. 1 to LTE and STE data (Lasič et al., 2014). The fitting procedure was not constrained to yield positive values for MD,  $V_I$  or  $V_A$ . Due to the variable density of data in each b-shell, we weighted the fitting to account for the heteroscedasticity of the powder averaged signal. The diffusional variance was reported in terms of a normalized metric, defined according to

$$MK_x = 3 \cdot \frac{V_x}{MD^2}, \quad \text{Eq. 3}$$

where ‘x’ denotes the isotropic, anisotropic or total diffusional variance, respectively. Westin et al. (2016) referred to these components as bulk, shear, and total kurtosis. Here, we refer them as components of the diffusional variance, since they reflect the variance of the DDC (Yablonskiy and Sukstanskii, 2010). Finally, we calculated the microscopic fractional anisotropy ( $\mu\text{FA}$ ), according to

$$\mu\text{FA} = \sqrt{\frac{3}{2}} \cdot \left(1 + \frac{MD^2 + V_I}{\frac{5}{2}V_A}\right)^{-1/2}, \quad \text{Eq. 4}$$

which can be interpreted as the FA that would be observed if all structures in the sample were aligned in parallel (Szczepankiewicz et al., 2016a, Westin et al., 2016). This means that the  $\mu\text{FA}$  captures the diffusional anisotropy even in samples that are isotropic on the voxel scale (Jespersen et al., 2013, Lawrenz et al., 2015, Szczepankiewicz et al., 2015).

### Analysis of repeatability

Repeatability was tested by acquiring data twice on systems A and D. On system A, the acquisitions were performed within the same session; on system D, acquisitions were separated by 20 days. Spatial correspondence across acquisitions was achieved by transforming the raw dMRI data into pre-MNI space, where data was resampled to 1.5 mm isotropic voxels to reduce smoothing effects from the interpolation. The transform to pre-MNI space was obtained from an affine registration of an FA volume (based on LTE with  $b < 1.2 \text{ ms}/\mu\text{m}^2$ ), to the FMRIB58 FA volume distributed in FSL (<http://fsl.fmrib.ox.ac.uk/>). We refer to this as the pre-MNI space, since only a linear transform was applied. To gauge the repeatability between the first and second acquisitions, we calculated the standard deviation (SD) of the difference between parameters calculated from repeated acquisitions, i.e.  $SD(X_1 - X_2)$ , where  $X$  denotes the parameter values in all included voxels (Bartlett and Frost, 2008). To avoid inflated uncertainty due to partially misaligned cortical regions, only voxels in the white matter were included by excluding voxels where  $\mu\text{FA} < 0.7$ .

### Signal to noise estimation

At very low SNR, the signal will be positively biased due to the rectified noise floor, with detrimental effects on parameter estimates (Jones and Basser, 2004, Dietrich et al., 2008). Since the STE was repeated several times for each b-value, we could estimate the SNR at each b-value by computing the ratio between the mean of the STE signal and its standard deviation. Assuming that the distribution of noise is approximately Rician, the noise floor bias is most prominent in regions where  $\text{SNR} < 3$ , as described by Gudbjartsson and Patz (1995). We use this threshold to detect regions where the noise floor is likely to bias the parameter estimation. As an additional gauge of data quality, we calculated the fraction of the brain volume where SNR was above 3 and 6 at  $b = 2 \text{ ms}/\mu\text{m}^2$ , denoted  $Q_3$

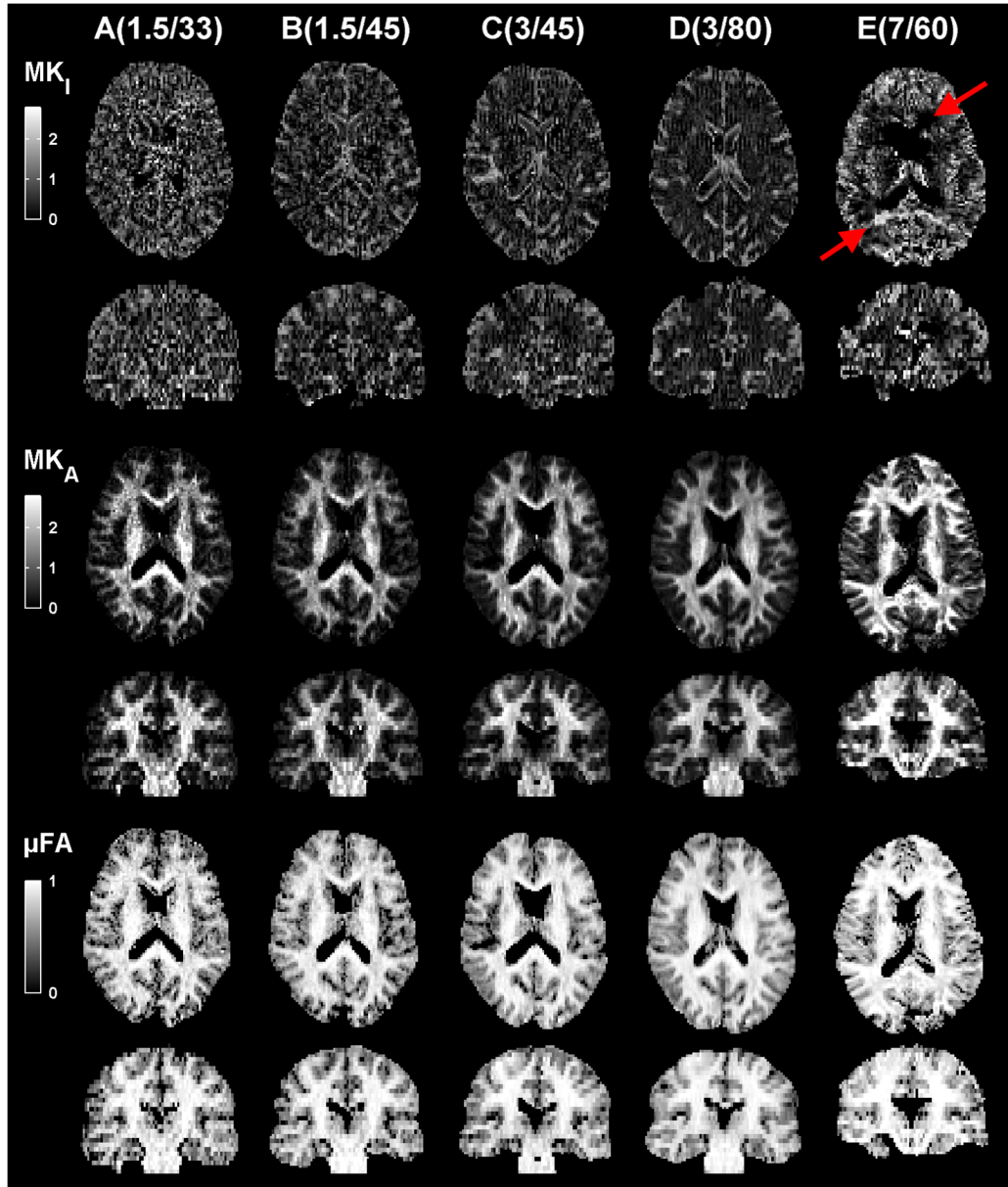


Figure 2 | Parameter maps in transversal and coronal slices, calculated from data acquired at five MRI systems (A-E, see Table 1) in one healthy volunteer. Generally, the image quality improves with field strength and gradient amplitude. Most notably there is a discernible increase in noise for systems A and B, as well as an apparent bias in the  $MK_I$  map. At the 7 T system (E), two notable artifacts appeared (red arrows); the anterior region exhibited negative  $MK_I$ , and in the posterior region we observed a prominent fat artefact. Furthermore, system E generally exhibited higher values of  $MK_A$  and  $\mu FA$  compared to the other systems.

and  $Q_6$ . Voxels where  $MD > 1.5 \mu m^2/ms$  were excluded to avoid partial volume effects with cerebrospinal fluid.

#### Simulation of parameter bias and precision

We investigated if noise could account for the observed parameter accuracy. The parameter bias and precision were investigated by simulations using three different sets of tissue parameters. All three sets had  $MD = 1 \mu m^2/ms$ . The first set had  $MK_I = 0.3$  and  $MK_A = 1.8$ , similar to the values detected in white matter at system D. The second set used reversed values ( $MK_I = 1.8$  and  $MK_A = 0.3$ ); no such values were detected in the healthy brain, but they may appear in tumor tissue (Szczepankiewicz et al., 2016a). The third set

assumed that  $MK_I = 0.0$  and  $MK_A = 1.8$  to test if signal noise can account for the non-zero  $MK_I$  that was detected in the white matter. The signal for each tissue was calculated from Eq. 1, and Rice distributed noise was added using the SNR estimated at each system. To represent a relatively noisy region, we estimated the SNR by placing an ROI in the corticospinal tract in an axial slice at the level of the lateral ventricles. Each system used the protocol described in Table 1 and the fitting was identical to that used in vivo, and was iterated 300 times using independent realizations of noise. The mean parameter across all iterations was calculated, along with the standard deviation and standard error of the mean.

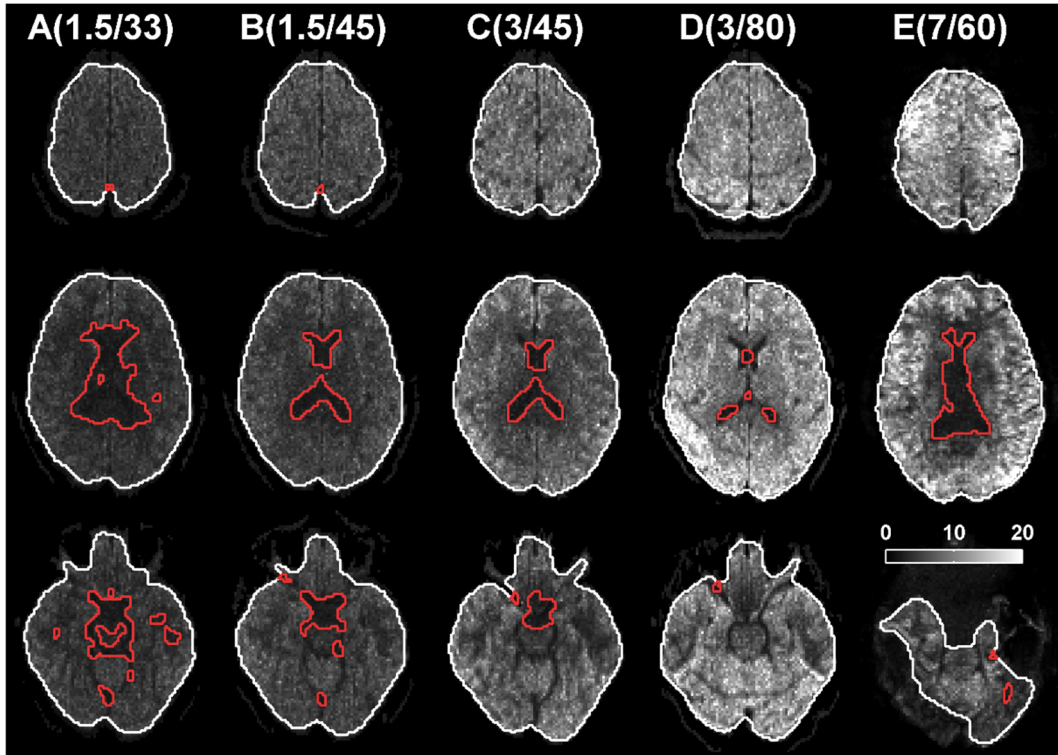


Figure 3 | SNR maps at  $b = 2 \text{ ms}/\mu\text{m}^2$  in three transversal slices, calculated from data acquired at five MRI systems (A-E, see Table 1) in one healthy volunteer. Red outlines show regions where  $\text{SNR} < 3$ ; white outlines show the outer limit where  $\text{SNR} > 3$ . On systems B-D the SNR was only low in regions with cerebrospinal fluid. System A showed low SNR in the central and inferior parts of the brain. System E generally exhibited high SNR in the peripheral regions and low SNR in proximity to the lateral ventricles and in the lower parts of the brain. The irregular brain outline in the lower part for system E was likely caused by poor RF homogeneity (Moser et al., 2012).

## Results

QTE was performed on all five systems, according to the protocols in Table 1, and Figure 2 shows the calculated DIVIDE parameter maps. There is an appreciable difference in image quality depending on hardware performance; as expected, higher  $B_0$  and higher  $G_{\text{max}}$  rendered higher quality images. The quality of the parameter maps was poorest on system A, where the influence of noise was evident in all parameters. This is likely due to the extended echo time ( $\text{TE} = 138 \text{ ms}$ ) incurred by the relatively low  $G_{\text{max}}$  of 33 mT/m. The parameter maps on system E ( $B_0 = 7 \text{ T}$ ) exhibited slightly different parameter contrast and were also noticeably affected by noise, and several image artifacts.

Figure 3 shows the estimated SNR at the highest b-value ( $b = 2 \text{ ms}/\mu\text{m}^2$ ) in three axial slices for all systems. The red outlines show regions where  $\text{SNR} < 3$ . Generally the SNR was highest in the peripheral parts of the brain, and relatively low in proximity to the lateral ventricles and in the inferior regions of the brain. Systems B-D exhibited  $\text{SNR} > 3$  in a majority of the brain ( $Q_3 > 95\%$ ). This was true also for system E, but only after regions with gross signal loss were excluded. Such signal dropout was likely explained by RF inhomogeneity, similar to that reported by

Sigmund and Gutman (2011). As expected, system A exhibited the lowest overall SNR, and did not achieve feasible SNR levels in the central parts of the brain ( $Q_3 = 88\%$  and  $Q_6 = 12\%$ ). A complete list of the quality parameters are reported in Table 1.

Figure 4 shows the simulated parameter estimation. The SNR at  $b = 0 \text{ ms}/\mu\text{m}^2$  was estimated to be 16, 22, 32, 53, and 34 at systems A-E, respectively. The results show an association between parameter precision and hardware performance, and that signal noise is a plausible cause for the parameter variations seen in the parameter maps. The precision in  $\text{MK}_I$  was consistently lower than for  $\text{MK}_A$ , regardless of their true values. Moreover, the simulations suggested that systems A and B exhibit a positive bias in  $\text{MK}_I$ , where the bias was 0.2 and 0.1, respectively. Remaining systems showed negligible bias ( $\text{MK}_I$  and  $\text{MK}_A$  differed less than 0.04 from the true value). The simulations where the true  $\text{MK}_I$  was set to zero indicated that noise could not account for non-zero  $\text{MK}_I$  at high SNR (system D), thus we attribute it to the presence of actual isotropic diffusional variance.

Data was also acquired on system A and D at resolutions of  $2.5 \times 2.5 \times 4 \text{ mm}^3$  and  $2 \times 2 \times 2 \text{ mm}^3$ , to address the low SNR at system A and to test the feasibility of a higher spatial resolution at system D. Figure 5 shows the

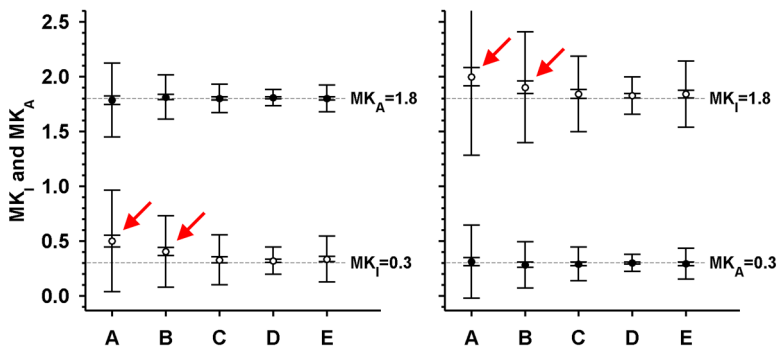


Figure 4 | Simulated effect of noise in two model tissues. Markers show the mean value; the outer whiskers show the standard deviation, and the inner whiskers show the standard error of the mean across 300 iterations of the simulation. The dashed horizontal lines show the true values used in the simulation. As expected, the parameter precision was highest for the systems that exhibited the highest SNR. Systems A and B exhibited positive bias in  $MK_I$  of 0.2 and 0.1 in both sets of tissue parameters (red arrows). The bias in  $MK_A$  was negligible at all systems.

resulting parameter maps and SNR maps. For system A, the reduction in spatial resolution resulted in improved SNR, where  $Q_3 = 99\%$  and  $Q_6 = 61\%$  compared to 88 and 12% for the original acquisition with  $2 \times 2 \times 4 \text{ mm}^3$  voxels. For system D, the increase in spatial resolution reduced the overall SNR, but the SNR remained high in most parts of the brain ( $Q_3 = 98\%$  and  $Q_6 = 59\%$ ). These results indicate that protocols with image resolutions tailored to systems with low or high performance are also technically feasible.

Figure 6 shows the repeatability analysis for systems A and D. The parameter maps for the first and second acquisition are qualitatively similar; parameter agreement is depicted as the difference between the first and second acquisition, and in Bland-Altman plots. The repeatability was higher on system D, and the  $MK_I$  consistently exhibits the highest uncertainty, in agreement with the simulations in Figure 4.

## Discussion

We have demonstrated that DIVIDE with QTE is technically feasible across a wide range of different MRI scanners, and we have shown examples of the parameter maps that can be expected at each system for acquisition times of 8 minutes. As expected, the system with strongest gradients (system D) rendered the highest SNR and image quality. However, the technical feasibility was also demonstrated at systems B-E, where at least 95% of the brain had  $\text{SNR} > 3$  (Table 1). By contrast, system A yielded the poorest SNR and image quality, where only 80% of the brain had  $\text{SNR} > 3$ . Accordingly, the parameter maps at system A were affected by the rectified noise floor. Additionally, the simulations indicated that system B may also exhibit a relevant parameter bias (Figure 4), especially in the central parts of the brain where SNR tended to be lower compared to peripheral tissue. Thus, the demand on  $\text{SNR} > 3$  may not be sufficient to avoid noise-floor effects in  $MK_I$ . Conversely, the simulations suggested that noise contributed negligible bias in  $MK_A$ , for all systems. Although system A initially failed to reach our criterion for

feasibility, we investigated the SNR and image quality also at a reduced spatial resolution. This yielded a feasible protocol with improved SNR and parameter map quality (Figure 5). Similarly, the superior SNR at system D facilitated a higher spatial resolution of 2 mm isotropic voxels, albeit at a prolonged scan time (Figure 5).

This study aimed at representing a wide range of MRI scanners, but hardware features other than those investigated herein may also affect image and parameter quality. For example, we cannot account for the effects of RF system, field heterogeneity, image acquisition and reconstruction, post-processing, and fitting procedure (Choi et al., 2011, Polders et al., 2011, Sigmund and Gutman, 2011, Moser et al., 2012). Furthermore, we acknowledge that the current results are based on a single healthy volunteer and may therefore lack generalizability to larger cohorts. However, we did demonstrate two aspects of technical robustness (Andersson, 1997). The test-retest data in Figure 6 demonstrated that our approach yields repeatable results within a single subject. Furthermore, we have previously demonstrated the technical robustness of the method in a proof-of-concept implementation (Sjölund et al., 2015), where QTE was performed in ten healthy volunteers at system C. Although that study used limited coverage (44 mm feet-head) and longer echo time ( $\text{TE} = 130 \text{ ms}$ ), the experiments yielded homogeneous data quality where  $Q_3 = 98 \pm 1\%$  and  $Q_6 = 52 \pm 10\%$ , similar to the current quality estimated at system C (Table 1). We consider also the present implementation at 7 T to be robust (system E), although only after exempting limitation that are characteristic to ultra-high fields, such as RF inhomogeneity, and unreliable fat suppression (Sigmund and Gutman, 2011, Moser et al., 2012). Moreover, our results indicate that  $MK_A$  was higher at 7 T compared to lower fields. The impact of this result on future studies is unclear and cannot be contrasted to literature since, to the best of our knowledge, no previous study has employed DKI or b-tensors of rank two or three at 7 T in vivo.

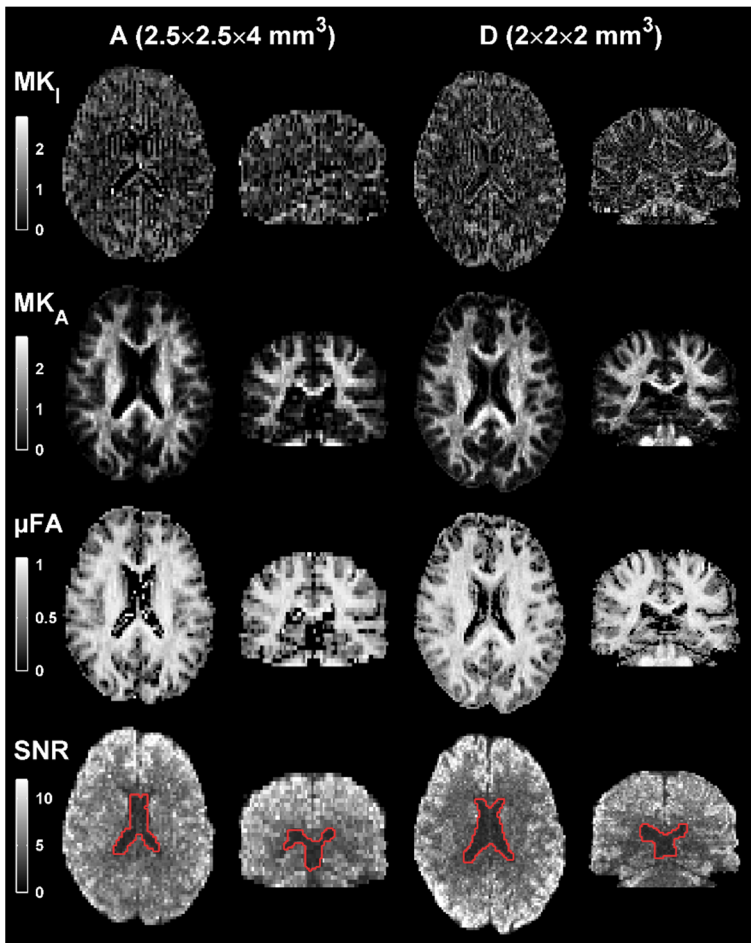


Figure 5 | Parameter and SNR maps at adjusted spatial resolution for systems A and D. The parameter maps from system A are markedly less noisy than at the initial resolution (Figure 2), and the SNR is above 3 in all regions where  $MD < 1.5 \mu\text{m}^2/\text{ms}$  ( $Q_3 = 99\%$ ,  $Q_6 = 61\%$ ). At system D the resolution was increased to 2 mm isotropic voxels, while maintaining sufficient SNR ( $Q_3 = 98\%$ ,  $Q_6 = 59\%$ ).

The feasibility of DIVIDE based on QTE hinges mainly on the use of optimized asymmetric gradient waveforms. The benefit of using the currently proposed waveforms and protocols can be appreciated by comparing them to the initial implementation which achieved a slice coverage of 15 mm in 10 minutes at an MRI scanner similar to system D (Szczepankiewicz et al., 2015). We estimate that using the previous waveform design at systems A, D, and E would render echo times of approximately 230, 140 and 170 ms, respectively. This translates to a relative SNR of 40%, 50% and 30%, assuming the white matter relaxation times presented by Cox and Gowland (2010). Asymmetric encoding has been explored previously for LTE and STE (Mori and van Zijl, 1995, Wong et al., 1995, Özarlan and Basser, 2008, Froeling et al., 2015), however, one should be aware that asymmetrical encoding also makes the imaging sequence sensitive to non-linear distortions of the gradient field, either due to non-linear gradient output or due to non-linear concomitant gradients (Bernstein et al., 1998, Baron et al., 2012). We did not observe any artifacts associated with concomitant gradient fields, however, they may impede accurate encoding at large field of views or with asymmetric gradient coils (Meier et al., 2008).

We emphasize that although this study demonstrates technical feasibility on a general level, investigation of the *clinical* feasibility, pertaining to specific applications, was outside the scope of this work. The present protocol design was intended for investigations of healthy brain tissue, and therefore accounts for the approximate diffusivity and anisotropy of brain tissue, as described in the Appendix. Naturally, a tissue with vastly different characteristics may require a different protocol. For example, a protocol designed for gliomas that exhibit  $MD \approx 1.8 \mu\text{m}^2/\text{ms}$  and  $FA \approx 0.1$  (Szczepankiewicz et al., 2016a) would generally entail a lower maximal b-value ( $b_{\text{max}} < 1.3 \text{ ms}/\mu\text{m}^2$ ) and fewer diffusion encoding directions ( $n_{\text{min}} = 3$ ); a markedly different premise for optimization compared to normal brain tissue (Appendix). A comprehensive protocol design should also consider the relaxation characteristics of the tissue. For example, transversal relaxation rates may depend on age and iron content, which may impact the SNR (Gelman et al., 1999, Siemonsen et al., 2008). Specific applications can also benefit substantially from adapting the image quality and scan time to the expected level of variance in the studied population (Szczepankiewicz et al., 2013), and we anticipate that simultaneous multi-slice

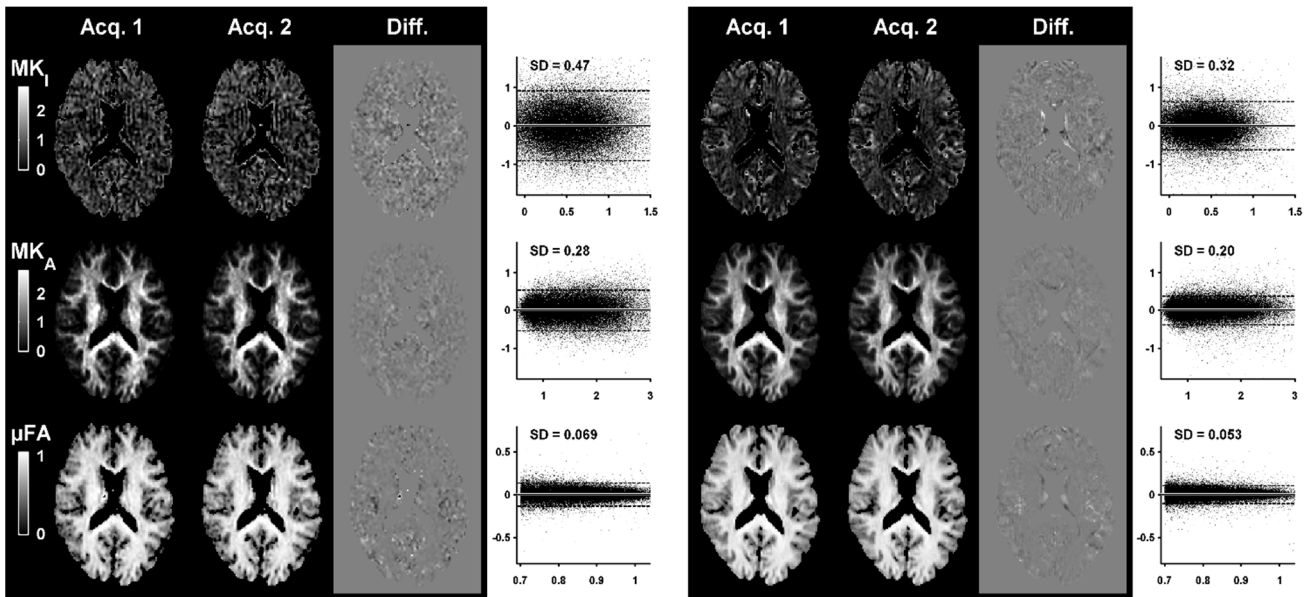


Figure 6 | Parameter maps from repeated experiments. The spatial resolution at system A was  $2.5 \times 2.5 \times 4 \text{ mm}^3$  (left), and at system D it was  $2 \times 2 \times 4 \text{ mm}^3$  (right). The repeatability is shown in terms of the voxel-wise difference (Diff.) between the first and second acquisition (Acq. 1 and 2). Bland-Altman plots are shown for each parameter; each data point represents a co-registered pair of voxels within the white matter. The x and y-axis of the plots show the difference and average, respectively; dashed lines show  $\pm 2 \cdot \text{SD}(X_1 - X_2)$ . Note that the SD pertains to voxel-wise parameter estimation. Analysis of the average across a larger region of interest can significantly improve the parameter precision.

techniques will provide a marked improvement of acquisition times (Setsompop et al., 2012).

We wish to highlight two limitations of the present study. First, we used asymmetric voxels ( $2 \times 2 \times 4 \text{ mm}^3$ ) as an effective means to increase the SNR and coverage of the protocols. Asymmetric voxels are known to introduce confounding effects in measures of voxel-wise diffusion anisotropy, for example in DTI, due to the interaction between voxel and structure geometry (Oouchi et al., 2007). By contrast, DIVIDE renders parameters that are independent of the orientation coherence of the underlying tissue, thus avoiding this limitation entirely (Lasič et al., 2014). However, other issues pertaining to asymmetric voxels remain, such as increased partial volume effects in the through-plane direction. Secondly, the DIVIDE approach assumes Gaussian diffusion in each micro-environment, i.e. that the diffusion is independent of the diffusion time. The diffusion process has been shown to be time-dependent in biological tissues using specialized diffusion encoding schemes (Stanisz et al., 1997, Assaf et al., 2000, Does et al., 2003, Fieremans et al., 2016), and in pathological tissue (Lätt et al., 2009). By contrast, studies performed at more conventional diffusion times in healthy tissue indicate that the effects are negligible (Clark et al., 2001, Ronen et al., 2006, Nilsson et al., 2009). The interplay between diffusion-time dependence and QTE waveforms is currently unknown, and further investigations are therefore warranted.

## Conclusions

Non-conventional diffusion encoding can probe microstructural features beyond those available with SDE. The preferred platform for in vivo experiments based on, for example, DDE, has been 3 T systems with high-performance gradients. In this study, we have demonstrated that QTE is technically feasible at a wide range of MRI systems, with main magnetic fields between 1.5 and 7 T, and gradient amplitudes as low as 33 mT/m. We have also demonstrated whole-brain DIVIDE in 8 minutes. The implementation was facilitated by efficient encoding waveforms and improved sampling protocols. By enabling QTE and DIVIDE at a wide range of systems, we expect that such methods may be more broadly used, which could open up new and exciting venues for dMRI research.

## Appendix – Protocol design

The design of the protocol followed three steps. Step (i), determine the minimal and maximal b-values ( $b_{\min}$  and  $b_{\max}$ ). An upper bound of the maximal b-value ( $b_{\max}$ ) was imposed by the assumption that the phase dispersion is approximately Gaussian (Lasič et al., 2014). This assumption is approximately valid if the signal is not attenuated below 10%, that is,  $S(b_{\max})/S_0 = \exp(-b \cdot \text{MD}) > 0.1$  (Topgaard and Söderman, 2003). Assuming a worst case scenario where STE renders monoexponential signal decay, we set the upper limit by requiring that

$$b_{\max} < -\frac{\ln(0.1)}{\text{MD}}. \quad \text{A. 1}$$

Thus, we get  $b_{\max} < 2.3 \text{ ms}/\mu\text{m}^2$  assuming  $\text{MD} \approx 1 \mu\text{m}^2/\text{ms}$  in brain tissue. The optimal value of  $b_{\max}$  depends on many factors, but in the context of DKI, it has been suggested that a reasonable value is  $b_{\max} = 2 \text{ ms}/\mu\text{m}^2$  (Jensen and Helpert, 2010, Hui and Jensen, 2015), which we adopted. The minimal b-value ( $b_{\min}$ ) is commonly set to zero, however, to reduce the influence of incoherent intra-voxel motion (Le Bihan et al., 1986), we set  $b_{\min} = 0.1 \text{ ms}/\mu\text{m}^2$ .

Step (ii), determine the TE, TR, and the number of samples. The TE was minimized under the constraint that the necessary  $b_{\max}$  was attainable by optimizing a waveform that produces the target b-tensor, and b-value, in the shortest time. This limit is typically set by the STE waveform. Several waveforms for STE exist (Mori and van Zijl, 1995, Wong et al., 1995, Moffat et al., 2005), however, we employed the optimized waveforms proposed by Sjölund et al. (2015). Subsequently, TR was determined from the TE and the number of slices.

Step (iii), distribute the samples in terms of sampling directions, b-values and tensor shapes. The total number of signal samples was  $\text{NOS} = T_{\text{tot}}/\text{TR}$ , where  $T_{\text{tot}}$  is the total scan time. The samples were distributed according to two considerations. First, we assume that the accuracy of the estimated  $V_1$  and  $V_A$  are equally important, thus the total number of samples were evenly distributed across LTE and STE. Second, the samples were distributed across three equidistant b-shells. If the requirement on rotationally invariant powder signal was fulfilled in each shell, an additional shell was added until no more samples remained. This was done iteratively, and the b-shells were always equidistant.

The minimum number of diffusion encoding directions required to yield a rotation invariant powder signal was estimated from simulations, according to the preliminary report by Szczepankiewicz et al. (2016c). Briefly, the simulations investigated the effects of rotation when using LTE in a system comprising a single diffusion tensor ( $\mathbf{D}$ ). The powder averaged signal ( $\bar{S}$ ) was calculated as the average diffusion-weighted signal along a number ( $n_{\text{dir}}$ ) of diffusion encoding directions ( $\mathbf{n}$ ,  $|\mathbf{n}| = 1$ ), according to

$$\bar{S}(b) = \frac{1}{n_{\text{dir}}} \sum_{i=1}^{n_{\text{dir}}} S_0 \exp(-b \cdot \mathbf{n}_i \mathbf{D} \mathbf{n}_i^T), \quad \text{A. 2}$$

where  $\mathbf{n}_i$  is the  $i^{\text{th}}$  direction in a set. This was done for 512 rotations of  $\mathbf{D}$ , which yielded as many realizations of the powder averaged signal, denoted  $\bar{S}_j(b)$ . The rotational variance was quantified in terms of the coefficient of

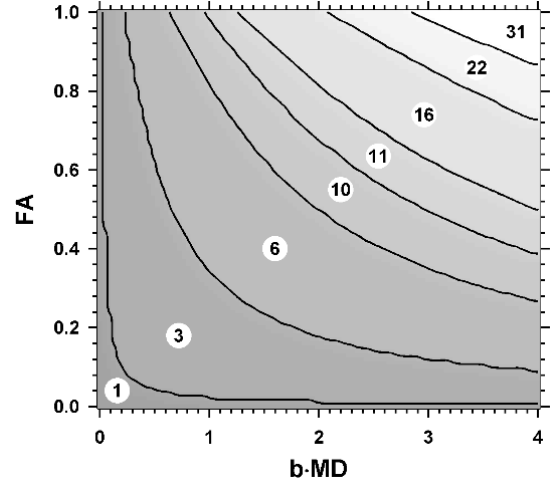


Fig. A. 1 | Minimal number of directions required ( $n_{\min}$ ) to yield a rotationally invariant powder averaged signal. The  $n_{\min}$  can be read from the figure for combinations of the tissue fractional anisotropy (FA) and attenuation factor ( $b \cdot \text{MD}$ ), where the numbers in the circles show  $n_{\min}$ . As expected, higher anisotropy and attenuation both demand a larger number of diffusion encoding directions. Note that rotational invariance is here assumed to be  $\text{CV} < 1\%$ .

variation (CV) of the powder averaged signal across all rotations, according to

$$\text{CV}(b) = \frac{\text{SD}(\bar{S}_j(b))}{\text{E}(\bar{S}_j(b))}, \quad \text{A. 3}$$

where  $\text{E}(\cdot)$  and  $\text{SD}(\cdot)$  are the operators for the mean and standard deviation, respectively. The CV was computed for  $n_{\text{dir}} \in [1, 64]$ . Each set of directions was independently optimized through electrostatic repulsion on the half-sphere (Jones et al., 1999, Leemans, 2009) where the optimization was repeated  $10^3$  times with random initialization to avoid sub-optimal direction sets (Cook et al., 2007). The threshold for rotation invariance was set to  $\text{CV} < 1\%$ . The minimum number of directions necessary to meet this condition ( $n_{\min}$ ) was calculated as a function of  $\text{FA} \in [0, 1]$  and  $b \cdot \text{MD} \in [0, 4]$ . The necessary number of directions are presented in Fig. A. 1. For example, coherent white matter where  $\text{MD} \approx 1 \mu\text{m}^2/\text{ms}$  and  $\text{FA} \approx 0.9$  requires  $n_{\min} = 16$  at  $b = 2 \text{ ms}/\mu\text{m}^2$ . For low b-values  $n_{\min}$  approaches 1, however, we set a minimum of at least 6 directions in each b-shell to reduce the potential influence from signal outliers. Note that a ‘minimal’ protocol using 3, 4 and 5 b-shells with linearly spaced  $b \in [0.1, 2] \text{ ms}/\mu\text{m}^2$  require at least 29, 36 and 46 LTE samples, respectively. For reference, assuming that  $\text{TR} = 5 \text{ s}$ , and with equal number of LTE and STE samples per b-shell, this amounts to  $T_{\text{tot}} \approx 5, 6, \text{ and } 8 \text{ minutes}$ .

## References

- Andersson, P. 1997. Robustness of Technical Systems in Relation to Quality, Reliability and Associated Concepts. *Journal of Engineering Design*, 8, 277-288.
- Assaf, Y., Mayk, A. & Cohen, Y. 2000. Displacement imaging of spinal cord using q-space diffusion-weighted MRI. *Magnetic Resonance in Medicine*, 44, 713-722.
- Assaf, Y. & Pasternak, O. 2008. Diffusion tensor imaging (DTI)-based white matter mapping in brain research: a review. *Journal of Molecular Neuroscience*, 34, 51-61.
- Bak, M. & Nielsen, N. C. 1997. REPULSION, A Novel Approach to Efficient Powder Averaging in Solid-State NMR. *Journal of Magnetic Resonance*, 125, 132-9.
- Baron, C. A., Lebel, R. M., Wilman, A. H. & Beaulieu, C. 2012. The effect of concomitant gradient fields on diffusion tensor imaging. *Magnetic Resonance in Medicine*, 68, 1190-201.
- Bartlett, J. W. & Frost, C. 2008. Reliability, repeatability and reproducibility: analysis of measurement errors in continuous variables. *Ultrasound in Obstetrics and Gynecology*, 31, 466-75.
- Basser, P. J., Mattiello, J. & Le Bihan, D. 1994. MR diffusion tensor spectroscopy and imaging. *Biophysical Journal*, 66, 259-67.
- Basser, P. J. & Pierpaoli, C. 1996. Microstructural and physiological features of tissues elucidated by quantitative-diffusion-tensor MRI. *Journal of Magnetic Resonance*, 209-2019.
- Bernstein, M. A., Zhou, X. J., Polzin, J. A., King, K. F., Ganin, A., Pelc, N. J. & Glover, G. H. 1998. Concomitant gradient terms in phase contrast MR: analysis and correction. *Magnetic Resonance in Medicine*, 39, 300-8.
- Callaghan, P. T. & Pinder, D. N. 1983. A Pulsed Field Gradient NMR-Study of Self-Diffusion in a Polydisperse Polymer System - Dextran in Water. *Macromolecules*, 16, 968-973.
- Chen, L., Liu, M., Bao, J., Xia, Y., Zhang, J., Zhang, L., Huang, X. & Wang, J. 2013. The correlation between apparent diffusion coefficient and tumor cellularity in patients: a meta-analysis. *PLoS ONE*, 8, e79008.
- Choi, S., Cunningham, D. T., Aguila, F., Corrigan, J. D., Bogner, J., Mysiw, W. J., Knopp, M. V. & Schmalbrock, P. 2011. DTI at 7 and 3 T: systematic comparison of SNR and its influence on quantitative metrics. *Magnetic Resonance Imaging*, 29, 739-51.
- Clark, C. A., Hedehus, M. & Moseley, M. E. 2001. Diffusion time dependence of the apparent diffusion tensor in healthy human brain and white matter disease. *Magnetic Resonance in Medicine*, 45, 1126-9.
- Cook, P. A., Symms, M., Boulby, P. A. & Alexander, D. C. 2007. Optimal acquisition orders of diffusion-weighted MRI measurements. *Journal of Magnetic Resonance Imaging*, 25, 1051-8.
- Cory, D. G., Garroway, A. N. & Miller, J. B. 1990. Applications of Spin Transport as a Probe of Local Geometry. *Abstracts of Papers of the American Chemical Society*, 199, 105.
- Cox, E. F. & Gowland, P. A. 2010. Simultaneous quantification of T2 and T2' using a combined gradient echo-spin echo sequence at ultrahigh field. *Magnetic Resonance in Medicine*, 64, 1440-5.
- Dietrich, O., Raya, J. G., Reeder, S. B., Ingrisch, M., Reiser, M. F. & Schoenberg, S. O. 2008. Influence of multichannel combination, parallel imaging and other reconstruction techniques on MRI noise characteristics. *Magnetic Resonance Imaging*, 26, 754-62.
- Does, M. D., Parsons, E. C. & Gore, J. C. 2003. Oscillating gradient measurements of water diffusion in normal and globally ischemic rat brain. *Magnetic Resonance in Medicine*, 49, 206-15.
- Edén, M. 2003. Computer simulations in solid-state NMR. III. Powder averaging. *Concepts in Magnetic Resonance Part A*, 18A, 24-55.
- Eriksson, S., Lasič, S., Nilsson, M., Westin, C. F. & Topgaard, D. 2015. NMR diffusion-encoding with axial symmetry and variable anisotropy: Distinguishing between prolate and oblate microscopic diffusion tensors with unknown orientation distribution. *Journal of Chemical Physics*, 142, 104201.
- Fieremans, E., Burcaw, L. M., Lee, H. H., Lemberskiy, G., Veraart, J. & Novikov, D. S. 2016. In vivo observation and biophysical interpretation of time-dependent diffusion in human white matter. *Neuroimage*.
- Froeling, M., Strijkers, G. J., Nederveen, A. J. & Luijten, P. R. 2015. Whole heart DTI using asymmetric bipolar diffusion gradients. *Journal of Cardiovascular Magnetic Resonance*, 17, P15.
- Gelman, N., Gorell, J. M., Barker, P. B., Savage, R. M., Spickler, E. M., Windham, J. P. & Knight, R. A. 1999. MR imaging of human brain at 3.0 T: preliminary report on transverse relaxation rates and relation to estimated iron content. *Radiology*, 210, 759-67.
- Gudbjartsson, H. & Patz, S. 1995. The Rician Distribution of Noisy MRI Data. *Magnetic Resonance Imaging*, 910-914.
- Ham, C. L., Engels, J. M., Van De Wiel, G. T. & Machielsen, A. 1997. Peripheral nerve stimulation during MRI: effects of high gradient amplitudes and switching rates. *Journal of Magnetic Resonance Imaging*, 7, 933-7.
- Hebrank, F. X. & Gebhardt, M. 2000. SAFE-Model - A New Method for Predicting Peripheral Nerve Stimulations in MRI. In: Proc. Intl. Soc. Mag. Res. Med., 2000.
- Hui, E. S. & Jensen, J. H. 2015. Double-pulsed diffusional kurtosis imaging for the in vivo assessment of human brain microstructure. *Neuroimage*, 120, 371-381.
- Jensen, J. H., Helpert, J. A., Ramani, A., Lu, H. & Kaczynski, K. 2005. Diffusional kurtosis imaging: the quantification of non-gaussian water diffusion by means of magnetic resonance imaging. *Magnetic Resonance in Medicine*, 53, 1432-40.
- Jensen, J. H. & Helpert, J. A. 2010. MRI quantification of non-Gaussian water diffusion by kurtosis analysis. *NMR in Biomedicine*, 23, 698-710.
- Jensen, J. H. 2014. Sufficiency of diffusion tensor in characterizing the diffusion MRI signal to leading order in diffusion weighting. *NMR in Biomedicine*, 27, 1005-7.
- Jespersen, S. N., Lundell, H., Sønderby, C. K. & Dyrby, T. B. 2013. Orientationally invariant metrics of apparent compartment eccentricity from double pulsed field gradient diffusion experiments. *NMR in Biomedicine*, 26, 1647-62.
- Jones, D. K., Horsfield, M. A. & Simmons, A. 1999. Optimal strategies for measuring diffusion in anisotropic systems by magnetic resonance imaging. *Magnetic Resonance in Medicine*, 42, 515-25.
- Jones, D. K. & Basser, P. J. 2004. "Squashing peanuts and smashing pumpkins": how noise distorts diffusion-weighted MR data. *Magnetic Resonance in Medicine*, 52, 979-93.
- Klein, S., Staring, M., Murphy, K., Viergever, M. A. & Pluim, J. P. 2010. elastix: a toolbox for intensity-based medical image registration. *IEEE Transactions on Medical Imaging*, 29, 196-205.
- Lasič, S., Szczepankiewicz, F., Eriksson, S., Nilsson, M. & Topgaard, D. 2014. Microanisotropy imaging: quantification of microscopic diffusion anisotropy and orientational order parameter by diffusion MRI with magic-angle spinning of the q-vector. *Frontiers in Physics*, 2, 11.

- Lawrenz, M., Brassens, S. & Finsterbusch, J. 2015. Microscopic diffusion anisotropy in the human brain: reproducibility, normal values, and comparison with the fractional anisotropy. *Neuroimage*, 109, 283-97.
- Le Bihan, D., Breton, E., Lallemand, D., Grenier, P., Cabanis, E. & Laval-Jeantet, M. 1986. MR imaging of intravoxel incoherent motions: application to diffusion and perfusion in neurologic disorders. *Radiology*, 161, 401-7.
- Le Bihan, D. 2013. Apparent diffusion coefficient and beyond: what diffusion MR imaging can tell us about tissue structure. *Radiology*, 268, 318-22.
- Leemans, A. 2009. ExploreDTI: a graphical toolbox for processing, analyzing, and visualizing diffusion MR data. *In: Proc. Intl. Soc. Mag. Reson. Med.*, 2009.
- Lätt, J., Nilsson, M., Van Westen, D., Wirestam, R., Ståhlberg, F. & Brockstedt, S. 2009. Diffusion-weighted MRI measurements on stroke patients reveal water-exchange mechanisms in sub-acute ischaemic lesions. *NMR in Biomedicine*, 22, 619-28.
- Meier, C., Zwanger, M., Feiweier, T. & Porter, D. 2008. Concomitant field terms for asymmetric gradient coils: consequences for diffusion, flow, and echo-planar imaging. *Magnetic Resonance in Medicine*, 60, 128-34.
- Mitra, P. 1995. Multiple wave-vector extensions of the NMR pulsed-field-gradient spin-echo diffusion measurement. *Physical Review B*, 51, 15074-15078.
- Moffat, B. A., Chenevert, T. L., Lawrence, T. S., Meyer, C. R., Johnson, T. D., Dong, Q., Tsien, C., Mukherji, S., Quint, D. J., Gebarski, S. S., Robertson, P. L., Junck, L. R., Rehemtulla, A. & Ross, B. D. 2005. Functional diffusion map: a noninvasive MRI biomarker for early stratification of clinical brain tumor response. *Proceedings of the National Academy of Sciences of the United States of America*, 102, 5524-9.
- Mori, S. & Van Zijl, P. 1995. Diffusion Weighting by the Trace of the Diffusion Tensor within a Single Scan. *Magnetic Resonance in Medicine*, 33, 41-52.
- Moser, E., Ståhlberg, F., Ladd, M. E. & Tractnig, S. 2012. 7-T MR—from research to clinical applications? *NMR in Biomedicine*, 25, 695-716.
- Nilsson, M., Lätt, J., Nordh, E., Wirestam, R., Ståhlberg, F. & Brockstedt, S. 2009. On the effects of a varied diffusion time in vivo: is the diffusion in white matter restricted? *Magnetic Resonance Imaging*, 27, 176-187.
- Nilsson, M., Szczepankiewicz, F., Van Westen, D. & Hansson, O. 2015. Extrapolation-Based References Improve Motion and Eddy-Current Correction of High B-Value DWI Data: Application in Parkinson's Disease Dementia. *PLoS ONE*, 10, e0141825.
- Oouchi, H., Yamada, K., Sakai, K., Kizu, O., Kubota, T., Ito, H. & Nishimura, T. 2007. Diffusion anisotropy measurement of brain white matter is affected by voxel size: underestimation occurs in areas with crossing fibers. *AJNR: American Journal of Neuroradiology*, 28, 1102-6.
- Polders, D. L., Leemans, A., Hendrikse, J., Donahue, M. J., Luijten, P. R. & Hoogduin, J. M. 2011. Signal to noise ratio and uncertainty in diffusion tensor imaging at 1.5, 3.0, and 7.0 Tesla. *Journal of Magnetic Resonance Imaging*, 33, 1456-63.
- Raab, P., Hattingen, E., Franz, K., Zanella, F. E. & Lanfermann, H. 2010. Cerebral gliomas: diffusional kurtosis imaging analysis of microstructural differences. *Radiology*, 254, 876-81.
- Ronen, I., Moeller, S., Ugurbil, K. & Kim, D. S. 2006. Analysis of the distribution of diffusion coefficients in cat brain at 9.4 T using the inverse Laplace transformation. *Magnetic Resonance Imaging*, 24, 61-8.
- Röding, M., Bernin, D., Jonasson, J., Sarkka, A., Topgaard, D., Rudemo, M. & Nyden, M. 2012. The gamma distribution model for pulsed-field gradient NMR studies of molecular-weight distributions of polymers. *Journal of Magnetic Resonance*, 222, 105-11.
- Röding, M., Williamson, N. H. & Nydén, M. 2015. Gamma convolution models for self-diffusion coefficient distributions in PGSE NMR. *Journal of Magnetic Resonance*, 261, 6-10.
- Setsompop, K., Cohen-Adad, J., Gagoski, B. A., Raij, T., Yendiki, A., Keil, B., Wedeen, V. J. & Wald, L. L. 2012. Improving diffusion MRI using simultaneous multi-slice echo planar imaging. *Neuroimage*, 63, 569-80.
- Shemesh, N., Özarslan, E., Komlosh, M. E., Basser, P. J. & Cohen, Y. 2010. From single-pulsed field gradient to double-pulsed field gradient MR: glean new microstructural information and developing new forms of contrast in MRI. *NMR in Biomedicine*, 23, 757-80.
- Siemonsen, S., Finsterbusch, J., Matschke, J., Lorenzen, A., Ding, X. Q. & Fiehler, J. 2008. Age-dependent normal values of T2\* and T2' in brain parenchyma. *AJNR: American Journal of Neuroradiology*, 29, 950-5.
- Sigmund, E. E. & Gutman, D. 2011. Diffusion-weighted imaging of the brain at 7 T with echo-planar and turbo spin echo sequences: preliminary results. *Magnetic Resonance Imaging*, 29, 752-65.
- Sjölund, J., Szczepankiewicz, F., Nilsson, M., Topgaard, D., Westin, C. F. & Knutsson, H. 2015. Constrained optimization of gradient waveforms for generalized diffusion encoding. *Journal of Magnetic Resonance*, 261, 157-168.
- Stanisz, G. J., Szafer, A., Wright, G. A. & Henkelman, R. M. 1997. An analytical model of restricted diffusion in bovine optic nerve. *Magnetic Resonance in Medicine*, 37, 103-11.
- Stejskal, E. O. & Tanner, J. E. 1965. Spin Diffusion Measurement: Spin echoes in the Presence of a Time-Dependent Field Gradient. *The Journal of Chemical Physics*, 42, 288-292.
- Szczepankiewicz, F., Lätt, J., Wirestam, R., Leemans, A., Sundgren, P., Van Westen, D., Ståhlberg, F. & Nilsson, M. 2013. Variability in diffusion kurtosis imaging: impact on study design, statistical power and interpretation. *Neuroimage*, 76, 145-54.
- Szczepankiewicz, F., Lasič, S., Van Westen, D., Sundgren, P. C., Englund, E., Westin, C. F., Ståhlberg, F., Lätt, J., Topgaard, D. & Nilsson, M. 2015. Quantification of microscopic diffusion anisotropy disentangles effects of orientation dispersion from microstructure: Applications in healthy volunteers and in brain tumors. *Neuroimage*, 104, 241-252.
- Szczepankiewicz, F., Van Westen, D., Englund, E., Westin, C. F., Ståhlberg, F., Lätt, J., Sundgren, P. C. & Nilsson, M. 2016a. The link between diffusion MRI and tumor heterogeneity: Mapping cell eccentricity and density by diffusional variance decomposition (DIVIDE). *Neuroimage*.
- Szczepankiewicz, F., Westin, C. F., Ståhlberg, F., Lätt, J. & Nilsson, M. 2016b. Microscopic Anisotropy Imaging at 7T Using Asymmetrical Gradient Waveform Encoding. *In: Proc. Intl. Soc. Mag. Reson. Med.* 24, 2016b Singapore. 1081.
- Szczepankiewicz, F., Westin, C. F., Ståhlberg, F., Lätt, J. & Nilsson, M. 2016c. Minimum number of diffusion encoding directions required to yield a rotationally invariant powder average signal in single and double diffusion encoding. *In: Proc. Intl. Soc. Mag. Reson. Med.* 24, 2016c Singapore. 2065.
- Topgaard, D. & Söderman, O. 2003. Experimental determination of pore shape and size using q-space NMR microscopy in

- the long diffusion-time limit. *Magnetic Resonance Imaging*, 21, 69-76.
- Topgaard, D. 2016. NMR methods for studying microscopic diffusion anisotropy. In: VALIULLIN, R. (ed.) *Diffusion NMR in Confined Systems: Fluid Transport in Porous Solids and Heterogeneous Materials*. Royal Society of Chemistry, Cambridge, UK.
- Van Cauter, S., Veraart, J., Sijbers, J., Peeters, R. R., Himmelreich, U., De Keyzer, F., Van Gool, S. W., Van Calenbergh, F., De Vleeschouwer, S., Van Hecke, W. & Sunaert, S. 2012. Gliomas: diffusion kurtosis MR imaging in grading. *Radiology*, 263, 492-501.
- Westin, C. F., Knutsson, H., Pasternak, O., Szczepankiewicz, F., Özarlan, E., Van Westen, D., Mattisson, C., Bogren, M., O'donnell, L. J., Kubicki, M., Topgaard, D. & Nilsson, M. 2016. Q-space trajectory imaging for multidimensional diffusion MRI of the human brain. *Neuroimage*, 135, 345-62.
- Wong, E. C., Cox, R. W. & Song, A. W. 1995. Optimized isotropic diffusion weighting. *Magnetic Resonance in Medicine*, 34, 139-43.
- Yablonskiy, D. A., Bretthorst, G. L. & Ackerman, J. J. 2003. Statistical model for diffusion attenuated MR signal. *Magnetic Resonance in Medicine*, 50, 664-9.
- Yablonskiy, D. A. & Sukstanskii, A. L. 2010. Theoretical models of the diffusion weighted MR signal. *NMR in Biomedicine*, 23, 661-81.
- Özarlan, E. & Basser, P. J. 2008. Microscopic anisotropy revealed by NMR double pulsed field gradient experiments with arbitrary timing parameters. *Journal of Chemical Physics*, 128, 154511.